POLITECNICO DI TORINO
Repository ISTITUZIONALE

Direct evidence for two-gap superconductivity in hydrogen-intercalated titanium diselenide

Original
Direct evidence for two-gap superconductivity in hydrogen-intercalated titanium diselenide / Piatti, E., Gavello, G., Ummarino, G.A., Košuth, F., Szabó, P., Samuely, P., Gonnelli, R.S., Daghero, D.. - In: MATERIALS TODAY PHYSICS. - ISSN 2542-5293. - STAMPA. - 59:(2025). [10.1016/j.mtphys.2025.101883]

Availability:
This version is available at: 11583/3003860 since: 2025-10-11T14:30:00Z

Publisher:
Elsevier

Published
DOI:10.1016/j.mtphys.2025.101883

Terms of use:

This article is made available under terms and conditions as specified in the corresponding bibliographic description in the repository

Publisher copyright

(Article begins on next page)

08 July 2026

Materials Today Physics 59 (2025) 101883

Contents lists available at ScienceDirect

Materials Today Physics

journal homepage: www.journals.elsevier.com/materials-today-physics

Direct evidence for two-gap superconductivity in hydrogen-intercalated titanium diselenide

Erik Piatti [a,*], Gaia Gavello [a], Giovanni A. Ummarino [a], Filip Košuth [b,c], Pavol Szabó [b], Peter Samuely [b], Renato S. Gonnelli [a,*], Dario Daghero [a]

[a] Department of Applied Science and Technology, Politecnico di Torino, I-10129 Torino, Italy
[b] Centre of Low Temperature Physics, Institute of Experimental Physics, Slovak Academy of Sciences, SK-04001, Košice, Slovakia
[c] Centre of Low Temperature Physics, Faculty of Science, P.J. Šafárik University, SK-04001, Košice, Slovakia

ARTICLE INFO

Keywords:
Transition metal dichalcogenides
$TiSe_2$
Multi-gap superconductivity
Hydrogen intercalation
Point-contact Andreev-reflection spectroscopy
Scanning tunneling spectroscopy

ABSTRACT

Transition-metal dichalcogenides (TMDs) offer an extremely rich material platform in the exploration of unconventional superconductivity. The unconventional aspects include exotic coupling mechanisms such as the Ising pairing, a complex interplay with other electronic orders such as charge-density waves (CDWs), symmetry-breaking and topological effects, and non-trivial gap structures such as multi-gap and possible nodal phases. Among TMDs, titanium diselenide ($1T$-$TiSe_2$) is one of the most studied and debated cases. Hints to an anomalous structure of its superconducting order parameter have emerged over the years, possibly linked to its texturing in real and reciprocal space due to the presence of a 2×2×2 CDW phase, or to a pressure-driven multi-band Fermi surface. However, direct evidence for an unconventional structure of the superconducting gap in this material is still lacking. In this work, the combination of the temperature dependence of the upper critical field with point-contact Andreev reflection and scanning tunneling spectroscopy measurements all consistently indicate the existence of two distinct superconducting gaps in the recently-discovered H-intercalated $TiSe_2$ superconductor. These results provide unambiguous evidence for a non-trivial superconducting phase in $TiSe_2$ and stimulate further research aimed at clarifying its connection with the orbital character and its interplay with the underlying CDW order.

1. Introduction

Transition metal dichalcogenides (TMDs) are a class of quasi-two-dimensional materials sharing the chemical fomula MX_2, where M is a transition metal and X is a chalcogen (S, Se, Te) atom, and exhibiting a layered crystal structure based on the stacking of covalently-bonded MX_2 trilayers which interact via weak inter-trilayer van der Waals forces [1]. Similarly to cuprates [2], heavy-Fermion [3] and iron-based [4,5] compounds, the vast chemical variety and complex electronic structures of TMDs often endow them with rich phase diagrams characterized by multiple quantum phases [6–8], the most commonly-occurring ones being superconductivity and charge-density waves (CDW) [9]. Additionally, the weak inter-layer bonding makes TMDs easily exfoliable down to the two-dimensional single-trilayer limit and eminently suited for chemical doping via intercalation of both atomic and molecular ions and neutral molecules [10,11]. This in turn provides ample control over their structural, electronic and optical properties, making TMDs remarkably appealing from both a fundamental and an application-oriented point of view [9,12–16].

Among TMDs, $1T$-$TiSe_2$ has been one of the most extensively investigated, starting from the discovery of a commensurate 2×2×2 CDW phase below ≈200 K in the undoped compound [17,18] whose origin is still a matter of debate [19–24]. Interest in this compound was further invigorated by the discovery that Cu intercalation could suppress the commensurate CDW order in favor of the emergence of a superconducting (SC) dome, with critical temperatures up to ≈ 4.15 K [25]. A similar tunability was later reported also in the case of applied pressure [26], electric-field-induced charge doping [27], and Pd [28], Li [29], H [30], and diamine [31] intercalation. Significant attention was devoted in particular to the possibility that the spatial texture associated with the CDW phase could affect the anisotropy of the SC pairing or even result in a non-trivial symmetry of the SC gap, especially after the observation of the Little-Parks effect in electrostatically-gated and Li-doped $TiSe_2$ indicated the existence of a periodic modulation in the amplitude of the SC order parameter [27,29].

* Corresponding authors.
E-mail addresses: erik.piatti@polito.it (E. Piatti), renato.gonnelli@polito.it (R.S. Gonnelli).

https://doi.org/10.1016/j.mtphys.2025.101883
Received 24 July 2025; Received in revised form 30 September 2025; Accepted 6 October 2025
Available online 10 October 2025
2542-5293/© 2025 The Authors. Published by Elsevier Ltd. This is an open access article under the CC BY license (http://creativecommons.org/licenses/by/4.0/).

Several works therefore aimed at probing the structure of the SC gap in $TiSe_2$. Most investigations have been carried out in the Cu-intercalated compound and concur in finding a single isotropic gap in the system [32–34]. Some exceptions to this general consensus have however been reported, usually in $TiSe_2$ systems where CDW and SC orders were simultaneously present and the amplitude of the latter might therefore be spatially textured: These include a possible two-gap state detected by μSR measurements in underdoped Cu_xTiSe_2 [35], a zero-bias peak at odds with isotropic *s*-wave pairing reported in the point-contact spectra of electrostatically-doped $TiSe_2$ [27], and a pronounced fluctuative regime with gap oscillations in magnetic fields observed in Li_xTiSe_2 by tunneling spectroscopy [36]. Unconventional $s_\pm$ pairing mediated by CDW fluctuations and driven by a Lifshitz transition has also recently been proposed to be responsible for superconductivity in pressurized $TiSe_2$, and possibly extend to the electron-doped compounds as well [37].

In this context, the recently-discovered H-intercalated $TiSe_2$ superconductor [30] is a prime candidate to host a non-trivial structure of the SC order parameter. This is because on the one hand the robust survival of CDW order detected at the intercalant sites by ^{1}H nuclear magnetic resonance [38] suggests a possible local coexistence of CDW and SC orders in the system; On the other hand, the large doping levels attained in H_xTiSe_2 (up to $x\approx2$) enable a full reconstruction of the Fermi surface by an orbital-selective filling of the Ti d_{z^2} band [30], mimicking that of SC TMD compounds NbS_2 and $NbSe_2$ where highly-anisotropic distributions of the SC gap on the Fermi surface [39,40] result in well known two-gap behaviors [41–47].

In this work, we present clear evidence for two-gap superconductivity in H-intercalated $TiSe_2$ revealed by directional point-contact Andreev-reflection spectroscopy (PCARS) and scanning tunneling spectroscopy (STS) measurements down to 0.3 K, by the temperature-dependence of the upper critical magnetic field determined by magnetotransport measurements, and their combined quantitative analysis within the two-band BCS and Eliashberg theory. We speculate that the two-gap structure may arise from an extremely anisotropic distribution of the SC gap function on the single Fermi surface of the material due to the orbital-selective filling induced by H intercalation.

2. Experimental methods

2.1. Ionic liquid gating-induced H intercalation

Flake-like 1*T*-$TiSe_2$ single crystals were purchased from HQ Graphene. Hydrogen intercalation was carried out by immersing the freshly-cleaved crystals (typical size $0.5\times0.5\times0.05\,mm^3$) in 1-ethyl-3-methylimidazolium tetrafluoroborate (Sigma Aldrich) and applying a gate voltage $V_G = +3.0$ V between them and a Pt counter-electrode using an Agilent B2961 power source, for ≈ 2 h and in ambient conditions. Higher voltages and temperatures were avoided to minimize the risk of undesired electrochemical interactions, such as intercalation of organic ions [48]. Intercalated crystals were thoroughly rinsed with acetone and ethanol and stored in a vacuum desiccator. Further details can be found in Ref. [30].

2.2. Electric transport measurements

The temperature-dependent resistivity was measured with the standard Van der Pauw method [49] in a Cryogenic Ltd ^{3}He insert loaded in a ^{4}He Oxford Instruments cryostat. The four-probe voltages were measured via Agilent 34420 nanovoltmeters upon excitation with a constant probe current ≈ 100 μA sourced via an Agilent B2912 source-measure unit, which was reversed during each measurement to remove common-mode offsets including thermoelectric voltages. The magnetic field was applied using a 9 T SC magnet and always kept orthogonal to the samples' *ab* plane.

2.3. Point-contact Andreev-reflection spectroscopy

PCARS measurements were carried out by means of the soft point-contact method [50] using the same experimental setup employed in the transport measurements. Small point-like contacts were realized on the intercalated $TiSe_2$ crystals by stretching thin Au wires on them so that they touched the freshly-cleaved surface only in a single point, and stabilizing the contact with Ag paste (RS Components) so that the measured conductance results from the parallel of several nanoscopic contacts. The differential conductance (dI/dV) spectra of the contacts were acquired by numerical differentiation of the $I-V$ (current–voltage) characteristic measured in the pseudo-four-probe configuration [51,52].

2.4. Scanning tunneling spectroscopy

The STS measurements were performed in a home-made low temperature STM setup, which was installed on the cold plate of a ^{3}He Cryomagnetics Inc system enabling measurements at temperatures down to 0.3 K and magnetic fields up to 8 T. The STM head allows all types of STM measurements and on multiple samples during one cooling. For the measurements we used an Au needle, which was formed by controlled collision on a massive piece of Au placed on the sample holder. The tunneling conductance spectra dI/dV were calculated by numerical differentiation from the $I-V$ curves. Prior to the experiments, the sample surfaces were cleaved by exfoliation and subsequently mounted into the STM head at ambient conditions over a period of about 20 min.

3. Results

3.1. Sample synthesis

Our magneto-transport and point-contact spectroscopy measurements were carried out on $TiSe_2$ single crystals which were intercalated with H atoms via the ionic liquid gating method [30,53]. As illustrated in Fig. 1a, the intense electric field at the voltage-polarized electrolyte/$TiSe_2$ interface dissociates the water molecules absorbed in the ionic liquid and injects the H^+ ions in the van der Waals gap of the layered crystal [54,55], while the gating time is used as a knob to control the amount of non-volatile H incorporation (Methods). Fig. 1b displays the resulting effects on the temperature (T) dependence of the in-plane resistivity, $\rho(T)$. Namely, H doping strongly suppresses the resistivity anomaly around ~160 K typical of undoped $TiSe_2$ crystals (solid brown line), which occurs as CDW order partially gaps the Fermi surface [25,27,28]; It also induces a more conventional metallic behavior in H_xTiSe_2 (solid blue line) and the development of a SC transition below 4 K. These effects are accompanied by electron doping which removes the CDW-driven sign change in the Hall coefficient around ~215 K [17,21,29,30]. Despite the loss of these transport anomalies, residual CDW ordering persists in the H-doped crystals as evidenced by the strong T-dependence of the Hall density n_H [30] and the peculiar dynamics of the ^{1}H nuclear magnetic moments [38]. Additional details can be found in Ref. [30], which established gate-driven protonation to be a reliable tool to control the ground state and induce SC in 1*T*-$TiSe_2$. In the following, we will focus on H_xTiSe_2 crystals with $x \approx 2$ (i.e., the maximum attainable H doping [30]) and $n_H(4.2\,K) \approx 5\times10^{20}\,cm^{-3}$ (Supplementary Note 1); from a structural standpoint, X-ray diffraction indicates that, at this doping level, H_xTiSe_2 crystals retain the 1*T* structure, but display a 0.9% increment in the unit cell volume with respect to the undoped material and a pronounced increase in structural disorder [30].

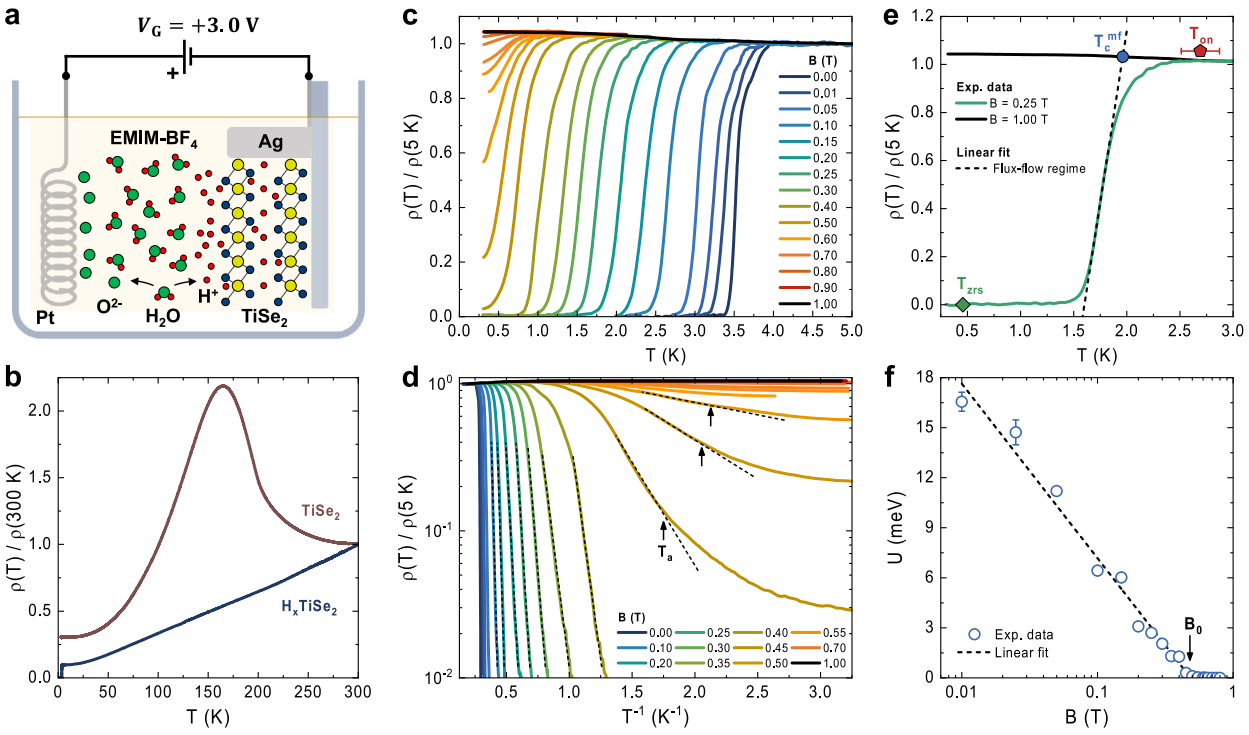

Fig. 1. Gate-driven H intercalation and superconductivity in $TiSe_2$. **a**, Schematic depiction of the experimental setup used in the gate-driven H intercalation process. The voltage V_G applied between the Pt gate electrode and the $TiSe_2$ crystal splits the water molecules absorbed by the EMIM-BF_4 ionic liquid and drives the H^+ ions inside the $TiSe_2$ structure. **b**, Resistivity ρ vs temperature T in pristine and H-intercalated $TiSe_2$ at zero magnetic field. **c**, $\rho(T)$ curves of H-intercalated $TiSe_2$ across the SC transition for increasing perpendicular magnetic fields B. **d**, same as **c** plotted in semilogarithmic scale against T^{-1}. Dashed lines are linear fits to the data which highlight the TAFF scaling. Arrows indicate the temperatures T_a where a crossover to pinning-free vortex motion occurs. **e**, $\rho(T)$ curve at $B = 0.25$ T with three characteristic T scales explicitly indicated: The zero-resistance state temperature T_{zrs}, the mean-field critical temperature T_c^{mf}, and the onset temperature T_{on}. The error bar represents the uncertainty on T_{on} due to the experimental resolution on the condition $d\rho/dT = 0$. The dashed line is a linear fit to the data in the flux-flow regime. The normal-state $\rho(T)$ curve at $B = 1$ T is also reported. **f**, B dependence of the activation barrier for vortex motion U in semilogarithmic scale, obtained from the slope of the linear fits shown in **d**. The corresponding statistical uncertainties are reported as error bars. The dashed line is a linear fit to the data.

3.2. Magneto-transport

We first focus on the response of the SC resistive transition of H_xTiSe_2 to the application of magnetic fields B perpendicular to the ab planes of the crystal. Fig. 1c shows $\rho(T)$ normalized to its value at 5 K, for zero and finite B in linear scale. When $B = 0$, the resistive transition reaches its midpoint – i.e., the T where $\rho(T)$ becomes half of its normal-state value – at 3.53 K, and drops below the noise level at $T_{zrs} = 2.9 \pm 0.2$ K, entering the zero-resistance state (ZRS). On increasing B, the resistive transitions are shifted to lower T and progressively broadened, likely owing to thermal phase fluctuations promoted by the inhomogeneous and quasi-2D character of the system [56,57]; nevertheless, a well-defined ZRS persists up to $B = 0.25$ T, whereas at higher fields dissipation is observed even at the lowest T accessible in our setup (0.3 K). The normal-state $\rho(T)$ curve, attained at $B = 1$ T, displays a slight upturn: its insensitivity to the applied B suggests that it cannot be ascribed to weak localization [58] or Kondo effect [59], but rather to the electronic correlations [60,61] arising from the localized Ti d orbitals [62,63]. As highlighted by the dashed lines in Fig. 1d, which plots $\rho(T)/\rho(5\,\mathrm{K})$ in semilogarithmic scale as a function of T^{-1}, the dissipative regime can be well-described in terms of thermally-activated flux flow (TAFF) of vortices, $\rho(B,T) = \rho_0 \exp\left[-U(B)/k_B T\right]$, where $U(B)$ is the potential barrier to vortex motion created by the pinning centers [64]. With respect to our earlier findings in the same system [30], however, the lower temperatures investigated here allow us to observe a range of T and B where $\rho(T)$ remains larger than predicted by the TAFF model, and we define $T_a(B)$ as the onset of this departure.

An accurate determination of the $B-T$ phase diagram of layered superconductors also requires an estimation of the T-dependence of the magnetic field of SC onset, $B_{on}(T)$, and of the mean-field upper critical field, $B_{c2}^{mf}(T)$. The $B_{on}(T)$ curve can be constructed by determining the crossing points between the $\rho(B)$ isotherms obtained by matrix inversion of the $\rho(T)$ curves [67,68] (see Supplementary Note 2) or, equivalently, by plotting the field dependence of the onset critical temperature, $T_{on}(B)$, defined as the value of T at which, for any given field B, $d\rho/dT = 0$ [56]. The $B_{c2}^{mf}(T)$ curve is especially necessary for a proper understanding of the vortex state and for the assessment of the gap symmetry. In 2D and highly-anisotropic superconductors, the SC transition is often smeared by thermal fluctuations and inhomogeneities, which in turn make commonly-used criteria (such as taking the point where the resistivity is 90% of the normal-state one) unreliable [56,69]. Therefore, we adopted the approach by Berghuis and Kes [65] and linearly extrapolated the resistivity in the flux-flow regime to the normal state. Doing so on the $\rho(B)$ isotherms (as exemplified in Supplementary Note 2) directly gives the $B_{c2}^{mf}(T)$ curve, while using the $\rho(T)$ curves at fixed B (as shown Fig. 1e for $B = 0.25$ T) provides the $T_c^{mf}(B)$ curve.

Fig. 2 displays the resulting comprehensive B–T phase diagram, which comprises different regions bounded by the zero-resistance curve ($T_{zrs}(B)$, green diamonds), the mean-field critical curve ($T_c^{mf}(B)$ and $B_{c2}^{mf}(T)$, filled and hollow blue circles), and the two crossover curves associated with the SC onset ($T_{on}(B)$ and $B_{on}(T)$, filled and hollow red pentagons) and the departure from TAFF vortex motion ($T_a(B)$, orange triangles) respectively. Both $T_{on}(B)$ and $B_{on}(T)$ lie well above the mean-field curve, indicating that a large region exists between the onset of

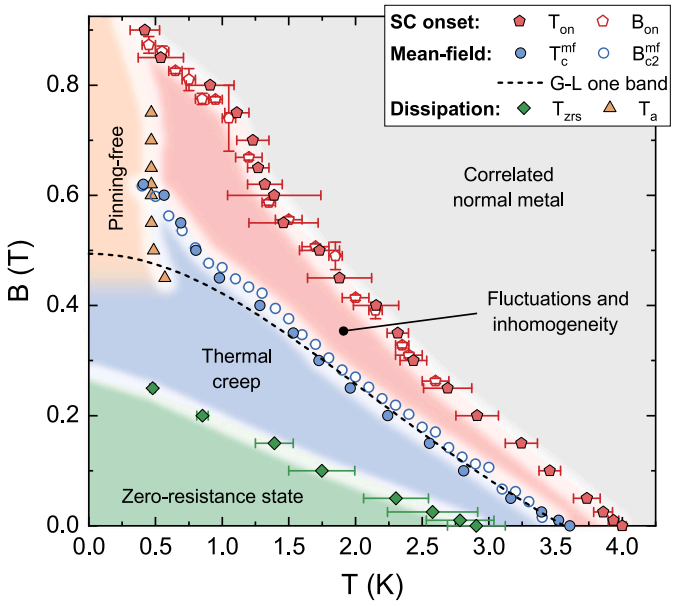

Fig. 2. Magnetic field-temperature (B–T) phase diagram of H-intercalated $TiSe_2$ determined from the magneto-transport measurements. T_{zrs} (green diamonds) are the temperatures below which zero resistance is observed. T_a (orange triangles) mark the boundary for the dissipative state due to pinning-free vortex motion. T_{on} and B_{on} (filled and open red pentagons) show the SC onset as defined by $d\rho/dT = 0$ and the crossing points of the $\rho(B)$ isotherms, respectively. T_c^{mf} and B_{c2}^{mf} (filled and open blue circles) represent the mean-field upper critical field determined by linear extrapolation to the normal state of the $\rho(T)$ and $\rho(B)$ curves, respectively [65]. Error bars are the resolution on the definitions due to the experimental noise level. The black dashed line shows the expected mean-field line according to the one-band Ginzburg–Landau model [66]. The truly dissipationless SC state is observed for $T \leq T_{zrs}$ (green region). Dissipation develops due to thermal creep at moderate B below the mean-field line (blue region) and free vortex motion at large B where the pinning potential is suppressed at low T (orange region). Inhomogeneity and amplitude fluctuations dominate between the mean-field line and the SC onset (red region).

SC fluctuations and the actual mean-field transition – as commonly observed in quasi-2D superconductors. The interval between the onset field and the mean-field one increases as T is reduced, which is not expected for pure thermal fluctuations of the order parameter amplitude [69,70] and indicates an important role played by an underlying mesoscopic inhomogeneity [57,71,72], possibly assisted by quantum fluctuations as B is increased [56]. The region between the mean-field line and the ZRS line is instead dominated by collective flux creep (thermal phase fluctuations) [64]: This is evidenced by the fact that the B dependence of the activation barrier for vortex motion scales as $U(B) = U_0 \ln(B_0/B)$ (as shown in Fig. 1f) with $U_0 = 53 \pm 2$ meV and $B_0 = 0.48 \pm 0.06$ T, comparable to earlier reports in both ion-gated [57] and H-doped [30] $TiSe_2$. Thermal creep therefore breaks down when $U(B) \to 0$ for $B \gtrsim B_0$, which indeed corresponds to the pocket below the $T_a(B)$ curve: This implies that the pinning potential effectively vanishes at high B, leading to a pinning-free motion of vortices which we ascribe to a combination of finite excitation current, high-frequency noise, and quantum fluctuations [73].

Finally, we focus on the mean-field critical curve. As already observed [56], the mean-field critical temperature T_c^{mf} is close to the midpoint of the resistive transition in $\rho(B)$ when $B \to 0$ but, on increasing B, it approaches the value of T where ρ is 95% of the normal-state value. Moreover, the mean-field line retains an upward curvature in the whole T range, exactly as the onset curve. This behavior is at odds with what observed in gated ZrNCl [56] where the SC onset curve displayed a low-T upturn, but the mean-field curve exhibited a clear downward curvature, compatible with the Wertharmer–Helfand–Hohenberg (WHH) theory. Incidentally, this means that, in our system, the upward curvature of the SC onset line is not (only) due to the effects of inhomogeneities and fluctuations as in ZrNCl, but reflects an intrinsic property of the material which already shows up in the T dependence of B_{c2}^{mf}. For $T < T_c/2$ such a T dependence is clearly incompatible with both the WHH theory and the standard one-band Ginzburg–Landau dependence $B_{c2} \propto (1 - t^2)/(1 + t^2)$, where $t = T/T_c$ [66] (black dashed line in Fig. 2). Conversely, positive curvatures in $B_{c2}(T)$ are usually a hallmark of superconductors where at least two effective SC gaps open on the Fermi surface [74–76].

3.3. Point-contact Andreev-reflection spectroscopy

We directly investigated the SC gap structure in our H_xTiSe_2 crystals by means of directional PCARS measurements [50,77] that we performed by means of the so-called soft technique (Methods). The direction of (main) current injection was controlled by making the point contacts either on the top surface (c-axis contacts) or the side (ab-plane contacts) of the platelet-like crystals. In both cases, we obtained conductance curves with spectroscopic signals only when the contacts where made immediately after cleaving (c axis) or breaking/cutting (ab plane) the crystals to minimize the exposure of the probed surfaces to air and moisture.

Fig. 3 shows two representative examples of differential conductance spectra (dI/dV vs V) of ab-plane point contacts (panels a,b) and c-axis point contacts (panels c,d). All the spectra were acquired at about 0.3 K and in zero magnetic field. The resistance of the contacts that allowed the detection of good spectroscopic signals is significantly different for the two directions, being much larger for ab-plane contacts ($R_N \gtrsim 500\,\Omega$) than for c-axis ones ($R_N \simeq 10\,\Omega$). All the spectra display zero-bias dips that are suggestive of nodeless SC gaps; in no cases we obtained the zero-bias peaks or cusps that are typical of nodal gaps or even gaps with zeros [50,52]. The two low-energy conductance maxima (indicated by green arrows) can definitely be associated to a SC gap, but these are not the only feature of the curves. Indeed, they all show additional structures, in the form of smooth shoulders or kinks (indicated by purple arrows) which can be interpreted as the hallmark of another gap. Similar structures were indeed often found in multigap superconductors like MgB_2 [78,79] and iron-based compounds [51,52,80]. It can be clearly seen that these features occur approximately at the same energy irrespective of the direction of current injection and of the contact resistance, which indicates their intrinsic nature.

Additional structures, indicated by red arrows, can also be identified. In the case of c-axis contacts, the shape of these structures allows identifying them with the typical "dips" that arise when the contact is not in the purely ballistic regime and are observed when the current density in the contact becomes overcritical, locally driving the superconductor in the resistive state [50,81,82]. In ab-plane contacts these dips are much weaker and occur at higher bias voltages, as expected due to the much larger resistance of the contacts; in Fig. 3a they even fall outside the voltage range.

Fig. 3e and f show the T dependence of the conductance curves in Fig. 3b and d. In either case, increasing T makes the amplitude of the Andreev signal decrease, while the two conductance maxima progressively shift to lower bias and then merge in a single hump at zero bias, as expected for gap amplitudes that decrease upon heating. The normal state is achieved when any trace of the low-energy conductance enhancement due to Andreev reflection disappears and subsequent curves collapse on a featureless spectrum. In both cases, a T-dependent downward shift of the high-energy tails of the curves can also be seen. This is due to the onset of the so-called spreading resistance [81,83,84], i.e. the resistance of the bulk of the crystal, that acts as an additional resistance in series to the contact in the proximity

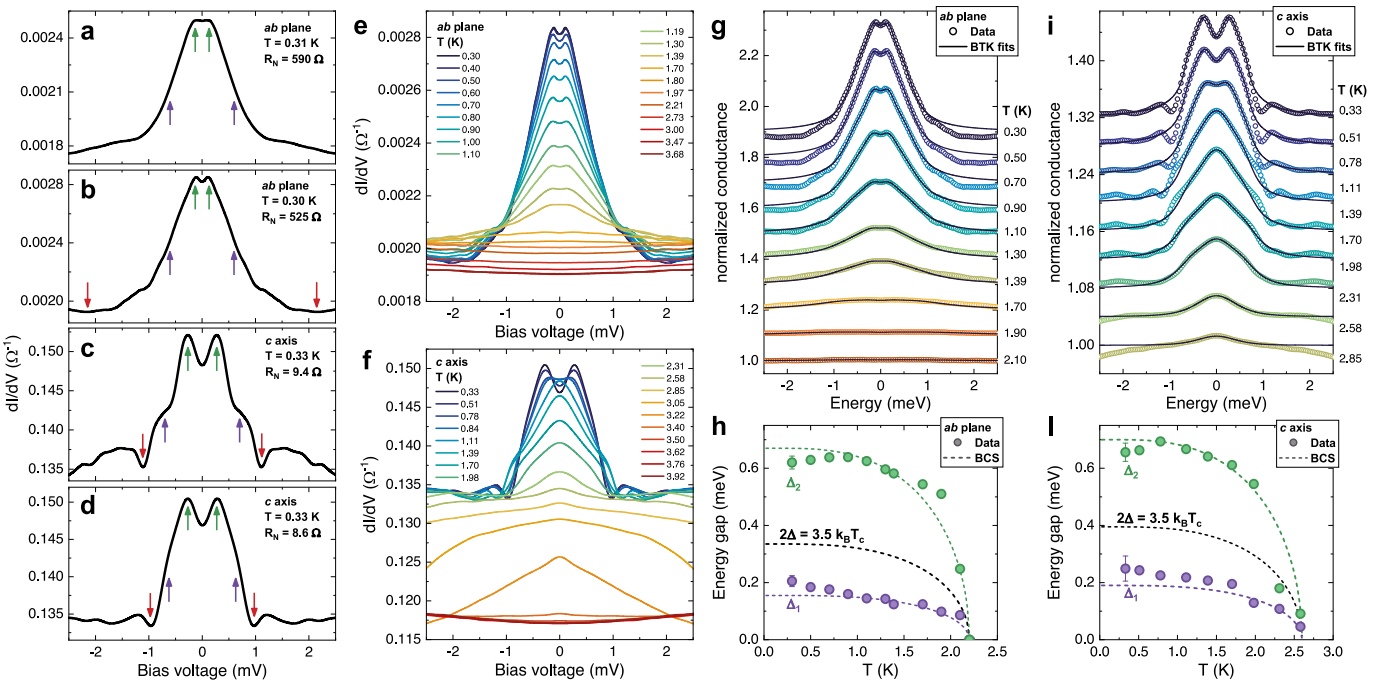

Fig. 3. Directional PCARS measurements in H_xTiSe_2. **a-d**, Examples of symmetrized differential conductance curves (dI/dV vs. V) measured in *ab*-plane (**a,b**) and *c*-axis (**c,d**) contacts. Normal-state resistance R_N and temperature T are indicated in the labels. Green, violed and red arrows highlight the spectral features associated to the small gap Δ_1, large gap Δ_2, and critical current "dips". **e,f**, T dependence of the dI/dV spectra displayed in panels **b,d**. **g**, Same curves of panel **e** after normalization (symbols) and the best-fitting curves (line) according to the two-band BTK model. **h**, T dependence of Δ_1 (purple circles) and Δ_2 (green circles) extracted from the fits in panel **g**. Dashed lines are functions of the form $\Delta_i(T) = \Delta_i(0)\tanh\left(1.74\sqrt{T_c^A/T-1}\right)$. **i,l**, Same as **g,h** for the curves of panel **f**.

of the resistive transition measured by transport (see Fig. 1c), as already pointed out elsewhere [52,85].

The fit of the curves in Fig. 3e and f is reported in Fig. 3g and i. The raw conductance spectra were symmetrized and normalized, i.e. divided by the normal-state conductance curve measured just above T_c and suitably corrected to get rid of the contribution of the spreading resistance [52,85]. The resulting experimental spectra were then fitted by using a 2D version [86,87] of the Blonder-Tinkham-Klapwijk (BTK) model [88] further generalized to the case of two isotropic (*s*-wave) energy gaps [50,78]. The model includes the gap amplitudes Δ_i, the broadening factors Γ_i, the interface barrier heights Z_i and the spectral weights of the two gaps w_i (bounded by $w_1+w_2 = 1$) as free parameters, which can be univocally set thanks to the different effect that each parameter plays in the shape of the curve [50,80]. We first tried to fit the curves with a single anisotropic gap, but we found that this model is unable to reproduce the shape of the spectra, especially in *c*-axis contacts (see Supplementary Note 3). As clearly seen in Fig. 3g and i, the two-gap model is instead able to grasp most of the features of the spectra, apart from those associated with the dips, which would require a more complicated model [81] as shown in Supplementary Note 4. The amplitude of the gaps is actually unaffected by whether we include the dip or not in the fit, which is a good check of internal consistency. The curves could be fitted only up to temperatures slightly above 2 K, because (as seen in Fig. 3e,f) above this value of T the spreading resistance starts to play a dominant role and the spectra, while being shifted downwards, are also stretched horizontally [81,83,84] preventing any spectroscopically-meaningful extraction of energy-resolved information.

The T dependence of the gap amplitudes, obtained through an automatic least-square procedure, are shown in Fig. 3h and l, whereas the Γ and Z parameters are summarized in Supplementary Note 5. The smaller gap Δ_1 decreases on increasing temperature, approximately following a BCS-like $\Delta(T)$ curve $\Delta_i(T) = \Delta_i(0)\tanh\left(1.74\sqrt{T_c^A/T-1}\right)$ (dashed purple line) – even though, instead of saturating at low temperature, below approximately 0.7 K it displays a linear behavior similar to that already observed in 1*H*-$NbSe_2$ by STS [89] and in $RbCa_2Fe_4As_4F_2$ by soft PCARS [52]. Surprisingly, the gap tends to zero well before the T_c^{mf} measured by transport, i.e. at $T_c^A \approx 2.2$ K in Fig. 3h and 2.6 K in Fig. 3l. This latter feature is common to *all* the contacts we made, irrespective of the direction of current injection, of the value of R_N and of the region of the crystal where the contact was made. Rather, these values are closer to the lower bound of the estimate for T_{zrs}, indicating a close link between T_c^A and the onset of TAFF. Notably, $T \approx 2$ K is also the temperature at which the superfluid density of H_xTiSe_2 vanished in muon-spin rotation measurements [30], which suggests that this suppression in T_c^A is not a surface effect but rather a bulk property of the material related to vanishing superfluid stiffness. The absolute values of Δ_1 are rather similar in the two directions, which excludes a large in-plane vs out-of-plane anisotropy of the order parameter. As for the larger gap Δ_2, it turns out to have a similar amplitude in *c*-axis and *ab*-plane contacts, always closes at the same T as Δ_1, and its T dependence is fairly similar to a BCS-like one, except for a weak maximum at low T and some deviations at higher T (where, actually, the large gap features are very weak and not well resolved). Concerning the gap spectral weights, we find $w_1 \approx 0.9$ for *c* axis contacts and ≈ 0.4 for *ab* plane contacts. Such directional anisotropy is typically expected in superconductors where the Fermi surface cannot be described by a simple sphere [50,80].

3.4. Scanning tunneling spectroscopy

To further assess the reliability of the PCARS results, we also carried out spectroscopic measurements in the pure tunneling regime, by using a scanning tunnel microscope (STM, see Methods). Even though the crystals were cleaved just before inserting them in the STM, a residual surface oxidation was detected, preventing the acquisition of conductance maps in STS mode. However, the home-built STM we used

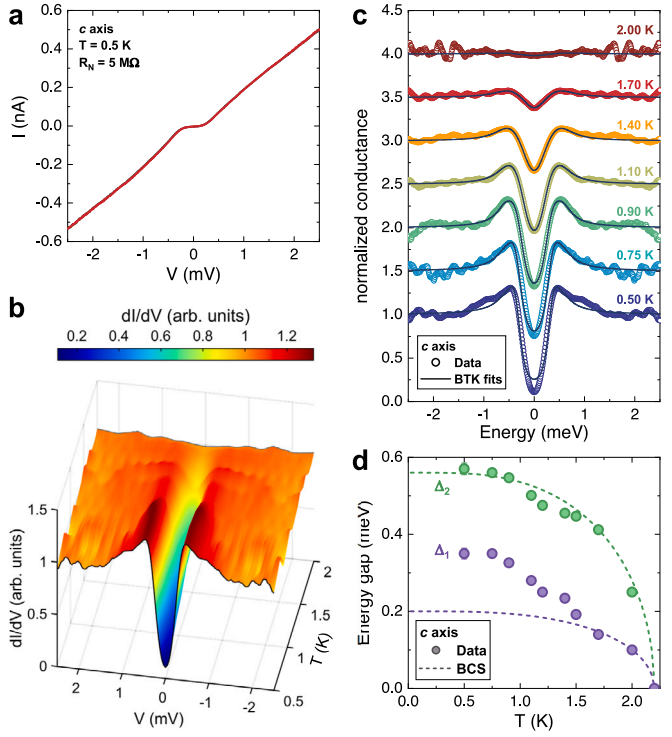

Fig. 4. Tunneling spectroscopy measurements in H_xTiSe_2. **a**, Example of an as-measured current–voltage ($I-V$) curve measured by biasing the sharp Au tip. **b**, Color plot of typical normalized STM tunneling spectra (dI/dV vs. V) measured at different temperatures T in zero magnetic field. **c**, Selected spectra from panel **b** (symbols) and best-fitting curves (lines) according to the two-band BTK model. **d**, T dependence of the superconducting gaps (symbols) extracted from the fits in panel **c**. Dashed lines are functions of the form $\Delta_i(T) = \Delta_i(0)\tanh\left(1.74\sqrt{T_c^A/T-1}\right)$.

also allows pushing the sharp Au tip of the microscope against the sample surface, thus piercing the damaged surface layer. After slightly retracting the tip, tunnel junctions with resistance of the order of $10^6\,\Omega$ were obtained on single locations of the sample, whose $I-V$ curves sometimes display an almost ideal tunnel behavior, as shown in Fig. 4a.

The differential conductance curves, $dI/dV(V)$, were obtained by numerical derivation from the $I-V$ curves, and then normalized by a linear background that fits their high-voltage tails (i.e. in a 1 mV-wide region around ±2.5 mV). Some examples of low-T normalized spectra are displayed in Supplementary Note 6. Fig. 4b shows instead the T dependence, up to 2 K, of the normalized (and symmetrized) differential conductance curves of one of the best junctions. The spectroscopic signal is very good and the SC gap is clearly visible. Again, in perfect agreement with the results of PCARS, the gap closes around 2 K.

A single-band Dynes fit is actually unable to fit the curves in an accurate way (Supplementary Note 7). We thus analyzed the same STS spectra by following the identical procedure we used for the PCARS ones, i.e. we fitted the symmetrized normalized conductance curves at various T by using the two-gap, 2D model for Andreev reflection at a S-I-N junction [50,78]. Fig. 4c shows that the result of the fit is very good at almost all temperatures up to 2 K. At the lowest T, the fitting function is able to reproduce the position and shape of the coherence peaks as well as the shape of the spectra at higher energies, but not the depth of the zero-bias dip. As a matter of fact, the low-bias shape of the tunnel curves display a change in slope that may suggest either a smaller gap *inside* the coherence peaks, or a broad distribution of gap amplitudes. The discrepancy is washed out by thermal broadening, so that at 1.10 K the fit is almost perfectly superimposed to the experimental curve. The gap amplitudes extracted from the fit of the T-dependent tunnel curves are shown in Fig. 4d. The large gap Δ_2 follows rather well a BCS-like T dependence (green dashed line) in the whole T range, whereas the small gap Δ_1 rather displays an almost linear trend that is poorly represented by a standard BCS-like curve. In particular, if the $\Delta_1(T)$ behavior close to T_c is thought to agree with a BCS-like curve (purple dashed line), as it happens in the case of PCARS data (see Fig. 3h,l), then the upward linear deviation on cooling starts already at 1.4 K. The weight of the small gap is here found to be $w_1 \approx 0.8$, in reasonable agreement with the PCARS value obtained in c axis contacts – although it must be noted that the weights do not have equivalent definitions in the Andreev and tunneling regimes [50,80].

4. Discussion

Both PCARS and tunneling spectroscopy measurements evidence the two-gap nature of the SC state of H_xTiSe_2. A summary of the low-T gap amplitudes obtained by PCARS and tunnel spectroscopy is shown in Fig. 5a. It is clearly seen that the gap amplitudes are spread within two well-separate energy ranges, highlighted by shaded bands, and are mostly independent of R_N, supporting the fact that the contacts are in the spectroscopic regime (at least at low T). Using the midpoint and half-width of these ranges as the experimental mean value and uncertainty of the gap amplitudes, one can extract $\langle\Delta_1\rangle = 0.26 \pm 0.12$ meV and $\langle\Delta_2\rangle = 0.62 \pm 0.18$ meV. The large spread suggests that there exists a spatial modulation of the gap amplitudes, and raises the question of whether the two gaps observed by tunnel and point-contact spectroscopies might simply originate from the intermixing of two spatially separate single-gap superconducting phases with different H doping and distinct energy gaps. This possibility can actually be excluded on the basis of several experimental evidences: (i) in each spectrum the two gaps close at the same temperature; (ii) one of them is systematically larger, and the other smaller, than the BCS value for a single-gap superconductor (see Figs. 3h and 3l), as it always happens in multi-gap superconductors [50,80]; (iii) the weight of the large-gap and small-gap contributions is almost the same in all the spectra, that were taken in different parts of the crystal. If the two gaps were due to different phases, one would expect a random, contact-dependent percentage of one phase or the other, which is not the case; (iv) tunnel spectroscopy is a local probe at atomic scale, and the measured spectra display features associated to both the gaps, clearly indicating that these exist in the same location.

Therefore, the more reasonable conclusion is that superconductivity in this compound has an intrinsic and local multi-gap nature. This said, it is still possible that the spatial inhomogeneity of the H content gives rise to a spatial modulation of the two gaps. In particular, soft PCARS probes a micrometric region of the sample and, if different spatially separate two-gap superconducting phases are intermixed, it may well collect signals coming from each of them. This can result in a smearing of the conductance peaks, which we cannot exclude (it is actually a reasonable source of the gap uncertainty). The difference in the gap amplitudes and T_c obtained from different contacts can be explained as well within this picture.

In Fig. 5b we plot the T dependence of the mean gap amplitudes (symbols), which we obtained by averaging the values determined from the BTK fits to the dI/dV spectra of all measured PCARS and STS contacts at each normalized temperature T/T_c. The average amplitudes of the large and small gap close at the same T_c and display BCS-like and quasi-linear T dependencies respectively – already observed in the spectra of individual contacts – which could explain the lack of saturation at low T detected in the superfluid density by muon spin rotation measurements [30]. All of these features can be fully captured by the theories for two-gap superconductivity, as confirmed by the excellent agreement between our data and the fits (solid and dashed lines, respectively) to both the Suhl-Matthias-Walker (SMW)

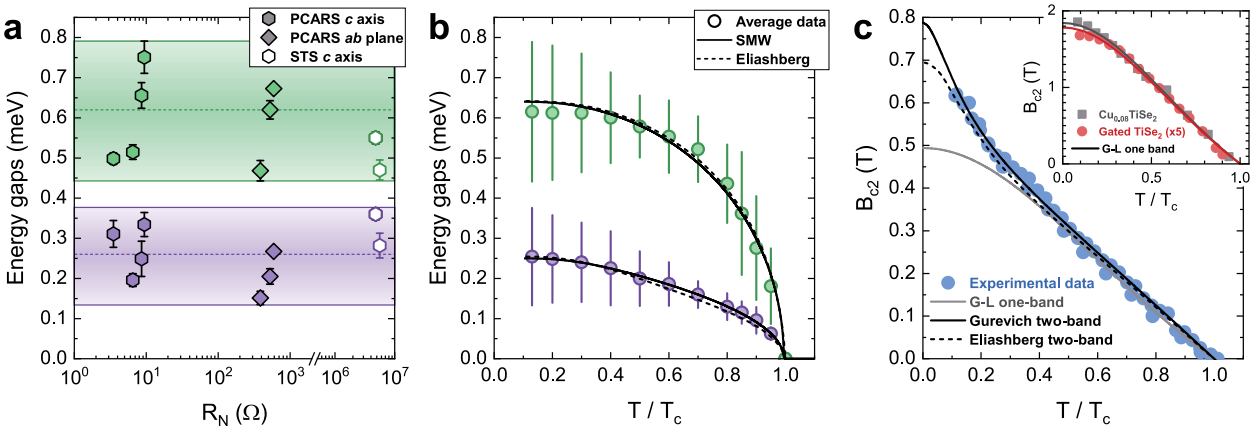

Fig. 5. Two-gap superconductivity in H_xTiSe_2. **a**, Energy gaps measured by PCARS (filled symbols) and STS (hollow symbols) as a function of the contact resistance R_N. Error bars are the spread of gap values obtained by using different normalization choices in the fitting procedure (Methods). **b**, Energy gaps as a function of normalized temperature (T/T_c). Symbols are the mean values obtained by averaging the data measured on all contacts at each T. Error bars are the corresponding spread between the different measurements. Solid and dashed lines are the fits with the SMW [90] and Eliashberg [91–93] two-band models. **c**, Upper critical field B_{c2} as a function of T/T_c. Symbols are the mean-field data shown in Fig. 2. Lines are fits to the one-band Ginzburg–Landau model [66] (solid gray line), the two-band Gurevich model [74–76] (solid black line) and the two-band Eliashberg model [94,95] (dashed black line). Inset shows B_{c2} vs. T/T_c for Cu_xTiSe_2 (grey squares, Ref. [25]) and ion-gated $TiSe_2$ (red circles, Ref. [27]) and the corresponding fits (solid lines) to the one-band Ginzburg–Landau model [66].

Table 1
Electron–phonon coupling matrix elements λ_{ij}, density of states ratio ν_{12}, total effective coupling constant λ_{eff}, diffusivity ratio η_{21}, and zero-temperature upper critical field $B_{c2}(0)$ calculated either with the weak-coupling SMW-Gurevich model or the strong-coupling Eliashberg model.

	λ_{11}	λ_{22}	λ_{21}	ν_{21}	λ_{eff}	η_{21}	$B_{c2}(0)$
SMW + Gurevich	0.14	0.22	0.06	0.48	0.34	12.4	0.79 T
Eliashberg	0.24	0.41	0.07	0.48	0.34	10.5	0.69 T

model based on two-band BCS theory [90] (Supplementary Note 8) and a more general model based on two-band Eliashberg theory [91–93] (Supplementary Note 9). The models allow determining the electron–phonon coupling matrix $\begin{pmatrix} \lambda_{11} & \lambda_{21}\nu_{21} \\ \lambda_{21} & \lambda_{22} \end{pmatrix}$ where $\nu_{21} = N_2(0)/N_1(0)$ is the ratio between the density of states at the Fermi level in the two bands. As summarized in Table 1, both models best fit the experimental data when: (i) the maximum coupling is the intraband term in the band associated to the large gap; (ii) a finite and non-negligible interband coupling is present; (iii) the density of states in the band associated to the large gap is nearly half that of the small gap. The individual values of the coupling constants cannot be directly compared between the two models since their definitions are not entirely equivalent; however, both models concur in finding a total effective coupling constant $\lambda_{eff} = 0.34$, indicating a marginal weak-coupling character for this compound.

The two-band models are able not only to account for the non-BCS, quasi-linear T dependence of the small gap, but also to reproduce the anomalous positive curvature of the T dependence of the upper critical field. As displayed in Fig. 5c, both the Gurevich model based on two-band BCS theory [74–76] (solid black line; see Supplementary Note 10) and the model based on two-band Eliashberg theory [94,95] (black dashed line; see Supplementary Note 11) are well matched with the B_{c2}^{mf} data obtained from the magnetotransport measurements in the entire T range. Notably, this excellent agreement is obtained by using the same coupling parameters that allowed reproducing the T dependence of the gaps in the weak- and strong-coupling models respectively, and both models find comparable values for $B_{c2}(0)$ and for $\eta_{21} = D_2/D_1$, the ratio between the diffusivities in the two bands. These findings set the hydrogen-induced SC state firmly apart from those induced in $TiSe_2$ by either electric field-driven charge doping [57] and Cu intercalation [25], where the T dependences of B_{c2} (red and black symbols in the inset to Fig. 5c respectively) display the conventional negative curvature commonly observed in superconductors with a single gap, and are well reproduced by the one-band Ginzburg–Landau model (solid lines).

Finally, we discuss possible origins for the two-gap SC state observed in $TiSe_2$ upon H intercalation but not upon other kinds of electron doping. At low T (and ambient pressure), the Fermi surface of undoped $TiSe_2$ is composed of six equivalent electron pockets located at the L points of the first Brillouin Zone and can thus be described by a single band [21,96]. Moderate electron doping levels, such as those corresponding to the SC phase induced by Cu intercalation, shift the Fermi level to higher energies but do not appreciably alter the band structure [30,97]. Conversely, the application of external pressure to $TiSe_2$ induces a SC phase in correspondence with an abrupt change in the Fermi surface topology (known as a Lifshitz transition) with the appearance of large additional hole pockets around the Γ point [37]. This makes the Fermi surface of pressurized $TiSe_2$ multi-band, with a comparable topology to that of Nb-based SC TMDs (NbS_2, $NbSe_2$) [41–47]. Since no sign of charge compensation due to hole pockets was observed in the Hall effect of H_xTiSe_2 [30], the most straightforward interpretation for our results would therefore be that H doping induces a Lifshitz transition in $TiSe_2$ to a Fermi surface composed of multiple inequivalent electron pockets – similar to the behavior displayed by electron-doped Mo- and W-based semiconducting TMDs (MoS_2, WS_2, $MoSe_2$, WSe_2) [76,98–100]. This simple interpretation is however at odds with the electronic band structure determined for H_xTiSe_2 via ab initio calculations, which predict that a single band crosses the Fermi level in the compound [30].

An alternative scenario is that the two-gap behavior of H_xTiSe_2 emerges from an extremely anisotropic distribution of the SC gap function in reciprocal space that is not correlated to the topology of the Fermi surface. In this picture, the two-gap model approximates the actual distribution of the SC gap with a function that takes two distinct constant values over different regions of the Fermi surface. Indeed, such a scenario was recently proposed to be responsible for the multi-gap properties of 2H-$NbSe_2$ [40], distinguishing it from the more conventional two-band behavior of the isostructural compound 2H-NbS_2 [39]. In $TiSe_2$, ab initio calculations showed that H intercalation leads to the filling of highly-coupled states with Ti d_{z^2} orbital character (not accessible with other types of electron doping) and to their hybridization with H-derived orbitals which partially screen phonon

perturbations, further enhancing their electron–phonon coupling [30]. Since the contribution of the Ti d_{z^2} states to the band structure is highly localized along the Γ–A line, we expect that this profound alteration of the orbital character of the electronic states at the Fermi level may act as an efficient source of gap anisotropy. In this picture, the effective two-gap behavior of H_xTiSe_2 would not be supported by a multi-*band* electronic structure, but rather a multi-*orbital* one enabled by the peculiar effects of H intercalation. Distinguishing between the different scenarios will require a direct probe of the Fermi surface, making measurements such as quantum oscillations or angle-resolved photoemission spectroscopy highly desirable in this compound.

5. Conclusions

In summary, we have investigated the structure of the superconducting order parameter in H-intercalated $TiSe_2$ by combining three techniques that independently probe the gap structure – magneto-transport, point-contact spectroscopy, and scanning tunneling spectroscopy measurements – yielding concording results and revealing the existence of two nodeless gaps. The spread in the gap values determined in different contacts suggests that their amplitude may be spatially modulated, but the local nature of the tunneling probe excludes that the two gaps might simply originate from phase separation. Furthermore, both the temperature dependence of gaps and of the upper critical magnetic field can be fitted extremely well by using BCS and Eliashberg models for two-band superconductivity, yielding coupling constants, density of states and diffusivity ratios in very good agreement. A comparison with the Fermiology of the system on the basis of ab initio calculations suggests that the two-gap structure may emerge from a multi-orbital single-band electronic structure rather than a more conventional multi-band Fermi surface. These facts further establish the effectiveness of gate-driven H intercalation to synthesize novel superconducting compounds with properties unattainable with conventional doping techniques.

CRediT authorship contribution statement

Erik Piatti: Writing – review & editing, Writing – original draft, Visualization, Methodology, Investigation, Funding acquisition, Formal analysis, Data curation, Conceptualization. **Gaia Gavello:** Writing – review & editing, Writing – original draft, Validation, Investigation, Formal analysis, Data curation. **Giovanni A. Ummarino:** Writing – review & editing, Methodology, Formal analysis. **Filip Košuth:** Writing – review & editing, Investigation, Formal analysis, Data curation. **Pavol Szabó:** Writing – review & editing, Supervision, Methodology, Investigation, Funding acquisition. **Peter Samuely:** Writing – review & editing, Supervision, Funding acquisition. **Renato S. Gonnelli:** Writing – review & editing, Writing – original draft, Supervision, Methodology, Investigation, Funding acquisition, Formal analysis, Conceptualization. **Dario Daghero:** Writing – review & editing, Writing – original draft, Supervision, Methodology, Investigation, Formal analysis, Conceptualization.

Declaration of competing interest

The authors declare that they have no known competing financial interests or personal relationships that could have appeared to influence the work reported in this paper.

Acknowledgments

E.P., D.D. and R.S.G. acknowledge support from the MIUR PRIN-2017 program (Grant No. 2017Z8TS5B – "Tuning and understanding Quantum phases in 2D materials – Quantum2D"). E.P. and R.S.G. also acknowledge funding by the European Union - Next Generation EU as part of the PRIN 2022 PNRR project "Continuous THERmal monitoring with wearable mid-InfraRed sensors" (P2022AHXE5). This publication is also part of the project PNRR-NGEU which has received funding from the MUR–DM 351/2022. The work at Slovak Academy of Sciences was supported by Projects APVV-23–0624, VEGA 2/0073/24, COST Action No. CA21144 (SUPERQUMAP) and Slovak Academy of Sciences Project IMPULZ IM-2021–42. We are thankful to G. Profeta, C. Tresca, G. Lamura and M. Bartoli for fruitful scientific discussions.

Appendix A. Supplementary data

Supplementary material related to this article can be found online at https://doi.org/10.1016/j.mtphys.2025.101883.

Data availability

Data will be made available on request.

References

[1] J.L.A. Wilson, A.D. Yoffe, The transition metal dichalcogenides discussion and interpretation of the observed optical, Electr. Struct. Prop. Adv. Phys. 18 (73) (1969) 193–335, http://dx.doi.org/10.1080/00018736900101307.

[2] K.M. Shen, J.S. Davis, Cuprate high-T_c superconductors, Mater. Today 11 (9) (2008) 14–21, http://dx.doi.org/10.1016/S1369-7021(08)70175-5.

[3] G.R. Stewart, Heavy-fermion systems, Rev. Modern Phys. 56 (4) (1984) 755, http://dx.doi.org/10.1103/RevModPhys.56.755.

[4] G.R. Stewart, Superconductivity in iron compounds, Rev. Modern Phys. 83 (4) (2011) 1589, http://dx.doi.org/10.1103/RevModPhys.83.1589.

[5] R.M. Fernandes, A.I. Coldea, H. Ding, I.R. Fisher, P. Hirschfeld, G. Kotliar, Iron pnictides and chalcogenides: a new paradigm for superconductivity, Nature 601 (35–44) (2022) 7891, http://dx.doi.org/10.1038/s41586-021-04073-2.

[6] S. Manzeli, D. Ovchinnikov, D. Pasquier, O.V. Yazyev, A. Kis, 2D transition metal dichalcogenides, Nat. Rev. Mater. 2 (8) (2017) 17033, http://dx.doi.org/10.1038/natrevmats.2017.33.

[7] W. Choi, N. Choudhary, G.H. Han, J. Park, D. Akinwande, Y.H. Lee, Recent development of two-dimensional transition metal dichalcogenides and their applications, Mater. Today 20 (3) (2017) 116–130, http://dx.doi.org/10.1016/j.mattod.2016.10.002.

[8] Y.W. Li, H.J. Zheng, Y.Q. Fang, D.Q. Zhang, Y.J. Chen, C. Chen, A.J. Liang, W.J. Shi, D. Pei, L.X. Xu, et al., Observation of topological superconductivity in a stoichiometric transition metal dichalcogenide 2M-WS_2, Nat. Commun. 12 (1) (2021) 2874, http://dx.doi.org/10.1038/s41467-021-23076-1.

[9] R.A. Klemm, Pristine and intercalated transition metal dichalcogenide superconductors, Phys. C: Supercond. Appl. 514 (2015) 86–94, http://dx.doi.org/10.1016/j.physc.2015.02.023.

[10] M.S. Dresselhaus, Intercalation in layered materials, MRS Bull. 12 (1987) 24–28.

[11] M.S. Stark, K.L. Kuntz, S.J. Martens, S.C. Warren, Intercalation of layered materials from bulk to 2D, Adv. Mater. 31 (27) (2019) 1808213, http://dx.doi.org/10.1002/adma.201808213.

[12] Q.H. Wang, K. Kalantar-Zadeh, A. Kis, J.N. Coleman, M.S. Strano, Electronics and optoelectronics of two-dimensional transition metal dichalcogenides, Nat. Nanotechnol. 7 (11) (2012) 699–712, http://dx.doi.org/10.1038/nnano.2012.193.

[13] A.K. Geim, I.V. Grigorieva, Van der Waals heterostructures, Nature 499 (7459) (2013) 419–425, http://dx.doi.org/10.1038/nature12385.

[14] G. Fiori, F. Bonaccorso, G. Iannaccone, T. Palacios, D. Neumaier, A. Seabaugh, S.K. Banerjee, L. Colombo, Electronics based on two-dimensional materials, Nat. Nanotechnol. 9 (10) (2014) 768–779, http://dx.doi.org/10.1038/nnano.2014.207.

[15] D. Voiry, A. Mohite, M. Chhowalla, Phase engineering of transition metal dichalcogenides, Chem. Soc. Rev. 44 (9) (2015) 2702–2712, http://dx.doi.org/10.1039/C5CS00151J.

[16] E. Piatti, A. Arbab, F. Galanti, T. Carey, L. Anzi, D. Spurling, A. Roy, A. Zhussupbekova, K.A. Patel, J.M. Kim, et al., Charge transport mechanisms in inkjet-printed thin-film transistors based on two-dimensional materials, Nat. Electron. 4 (12) (2021) 893–905, http://dx.doi.org/10.1038/s41928-021-00684-9.

[17] F.J. Di Salvo, D.E. Moncton, J.V. Waszczak, Electronic properties and superlattice formation in the semimetal $TiSe_2$, Phys. Rev. B 14 (10) (1976) 4321, http://dx.doi.org/10.1103/PhysRevB.14.4321.

[18] J.C.E. Rasch, T. Stemmler, B. Müller, L. Dudy, R. Manzke, 1T-$TiSe_2$: Semimetal or semiconductor? Phys. Rev. Lett. 101 (23) (2008) 237602, http://dx.doi.org/10.1103/PhysRevLett.101.237602.

[19] K. Rossnagel, L. Kipp, M. Skibowski, Charge-density-wave phase transition in 1T-$TiSe_2$: Excitonic insulator versus band-type Jahn-Teller mechanism, Phys. Rev. B 65 (23) (2002) 235101, http://dx.doi.org/10.1103/PhysRevB.65.235101.

[20] A. Kogar, M.S. Rak, S. Vig, A.A. Husain, F. Flicker, Y.I. Joe, L. Venema, G.J. MacDougall, T.C. Chiang, E. Fradkin, et al., Signatures of exciton condensation in a transition metal dichalcogenide, Science 358 (6368) (2017) 1314–1317, http://dx.doi.org/10.1126/science.aam6432.

[21] P. Knowles, B. Yang, T. Muramatsu, O. Moulding, J. Buhot, C.J. Sayers, E. Da Como, S. Friedemann, Fermi surface reconstruction and electron dynamics at the charge-density-wave transition in $TiSe_2$, Phys. Rev. Lett. 124 (16) (2020) 167602, http://dx.doi.org/10.1103/PhysRevLett.124.167602.

[22] M.R. Otto, J.-H. Pöhls, L.P. René de Cotret, M.J. Stern, M. Sutton, B.J. Siwick, Mechanisms of electron–phonon coupling unraveled in momentum and time: The case of soft phonons in $TiSe_2$, Sci. Adv. 7 (20) (2021) eabf2810, http://dx.doi.org/10.1126/sciadv.abf2810.

[23] Z. Lin, C. Wang, A. Balassis, J. Echeverry, A. Vasenko, V.M. Silkin, E.V. Chulkov, Y. Shi, J. Zhang, J. Guo, et al., Dramatic plasmon response to the charge-density-wave gap development in 1T-$TiSe_2$, Phys. Rev. Lett. 129 (18) (2022) 187601, http://dx.doi.org/10.1103/PhysRevLett.129.187601.

[24] D. Novko, Z. Torbatian, I. Lončarić, Electron correlations rule the phonon-driven instability in single-layer $TiSe_2$, Phys. Rev. B 106 (24) (2022) 245108, http://dx.doi.org/10.1103/PhysRevB.106.245108.

[25] E. Morosan, H.W. Zandbergen, B. Dennis, J. Bos, Y. Onose, T. Klimczuk, A. Ramirez, N. Ong, R.J. Cava, Superconductivity in Cu_xTiSe_2, Nat. Phys. 2 (8) (2006) 544–550, http://dx.doi.org/10.1038/nphys360.

[26] A.F. Kusmartseva, B. Sipos, H. Berger, L. Forro, E. Tutiš, Pressure induced superconductivity in pristine 1T-$TiSe_2$, Phys. Rev. Lett. 103 (23) (2009) 236401, http://dx.doi.org/10.1103/PhysRevLett.103.236401.

[27] L.J. Li, E.C.T. O'Farrell, K.P. Loh, G. Eda, B. Özyilmaz, A.H. Castro Neto, Controlling many-body states by the electric-field effect in a two-dimensional material, Nature 529 (2016) 185–189, http://dx.doi.org/10.1038/nature16175.

[28] E. Morosan, K.E. Wagner, L.L. Zhao, Y. Hor, A.J. Williams, J. Tao, Y. Zhu, R.J. Cava, Multiple electronic transitions and superconductivity in Pd_xTiSe_2, Phys. Rev. B 81 (9) (2010) 094524, http://dx.doi.org/10.1103/PhysRevB.81.094524.

[29] M. Liao, H. Wang, Y. Zhu, R. Shang, M. Rafique, L. Yang, H. Zhang, D. Zhang, Q.-K. Xue, Coexistence of resistance oscillations and the anomalous metal phase in a lithium intercalated $TiSe_2$ superconductor, Nat. Commun. 12 (1) (2021) 5342, http://dx.doi.org/10.1038/s41467-021-25671-8.

[30] E. Piatti, G. Prando, M. Meinero, C. Tresca, M. Putti, S. Roddaro, G. Lamura, T. Shiroka, P. Carretta, G. Profeta, et al., Superconductivity induced by gate-driven hydrogen intercalation in the charge-density-wave compound 1T-$TiSe_2$, Commun. Phys. 6 (1) (2023) 202, http://dx.doi.org/10.1038/s42005-023-01330-w.

[31] K. Sato, T. Noji, T. Hatakeda, T. Kawamata, M. Kato, Y. Koike, New lithium- and diamines-intercalated superconductors $Li_x(C_2H_8N_2)_yTiSe_2$ and $Li_x(C_6H_{16}N_2)_yTiSe_2$, J. Phys. Soc. Japan 86 (10) (2017) 104701, http://dx.doi.org/10.7566/JPSJ.86.104701.

[32] S.Y. Li, G. Wu, X.H. Chen, L. Taillefer, Single-gap s-wave superconductivity near the charge-density-wave quantum critical point in Cu_xTiSe_2, Phys. Rev. Lett. 99 (10) (2007) 107001, http://dx.doi.org/10.1103/PhysRevLett.99.107001.

[33] A.D. Hillier, P. Manuel, D.T. Adroja, J.W. Taylor, A.K. Azad, J.T.S. Irvine, Probing the superconducting ground state near the charge density wave phase transition in $Cu_{0.06}TiSe_2$, Phys. Rev. B 81 (9) (2010) 092507, http://dx.doi.org/10.1103/PhysRevB.81.092507.

[34] J. Kačmarčík, Z. Pribulová, V. Pal'uchová, P. Szabó, P. Husaníková, G. Karapetrov, P. Samuely, Heat capacity of single-crystal Cu_xTiSe_2 superconductors, Phys. Rev. B 88 (2) (2013) 020507, http://dx.doi.org/10.1103/PhysRevB.88.020507.

[35] M. Zaberchik, K. Chashka, L. Patlgan, A. Maniv, C. Baines, P. King, A. Kanigel, Possible evidence of a two-gap structure for the Cu_xTiSe_2 superconductor, Phys. Rev. B 81 (22) (2010) 220505, http://dx.doi.org/10.1103/PhysRevB.81.220505.

[36] J.-Y. Ji, Z. Cao, Y. Hu, H. Wu, H. Wang, Y. Zhu, H. Liu, L. Yang, Q.-K. Xue, D. Zhang, Superconducting gap and its Little-Parks-like oscillations with high-order harmonics in lithium intercalated 1T-$TiSe_2$, Nano Lett. 25 (26) (2025) 10641–10647, http://dx.doi.org/10.1021/acs.nanolett.5c02401.

[37] R.D.H. Hinlopen, O.N. Moulding, W.R. Broad, J. Buhot, F. Bangma, A. McCollam, J. Ayres, C.J. Sayers, E. Da Como, F. Flicker, J. Van Wezel, S. Friedemann, Lifshitz transition enabling superconducting dome around a charge-order critical point, Sci. Adv. 10 (27) (2024) eadl3921, http://dx.doi.org/10.1126/sciadv.adl3921.

[38] G. Prando, E. Piatti, D. Daghero, R.S. Gonnelli, P. Carretta, Cluster charge-density-wave glass in hydrogen-intercalated $TiSe_2$, Phys. Rev. Mater. 7 (9) (2023) 094002, http://dx.doi.org/10.1103/PhysRevMaterials.7.094002.

[39] C. Heil, S. Poncé, H. Lambert, M. Schlipf, E.R. Margine, F. Giustino, Origin of superconductivity and latent charge density wave in NbS_2, Phys. Rev. Lett. 119 (8) (2017) 087003, http://dx.doi.org/10.1103/PhysRevLett.119.087003.

[40] A. Sanna, C. Pellegrini, E. Liebhaber, K. Rossnagel, K.J. Franke, E.K.U. Gross, Real-space anisotropy of the superconducting gap in the charge-density wave material 2H-$NbSe_2$, Npj Quantum Mater. 7 (1) (2022) 6, http://dx.doi.org/10.1038/s41535-021-00412-8.

[41] I. Guillamón, H. Suderow, S. Vieira, L. Cario, P. Diener, P. Rodiere, Superconducting density of states and vortex cores of 2H-NbS_2, Phys. Rev. Lett. 101 (16) (2008) 166407, http://dx.doi.org/10.1103/PhysRevLett.101.166407.

[42] J. Kačmarčík, Z. Pribulová, C. Marcenat, T. Klein, P. Rodière, L. Cario, P. Samuely, Studies on two-gap superconductivity in 2H-NbS_2, Phys. C: Supercond. Appl. 470 (2010) S719–S720, http://dx.doi.org/10.1016/j.physc.2009.10.131.

[43] T. Yokoya, T. Kiss, A. Chainani, S. Shin, M. Nohara, H. Takagi, Fermi surface sheet-dependent superconductivity in 2H-$NbSe_2$, Science 294 (5551) (2001) 2518–2520, http://dx.doi.org/10.1126/science.1065068.

[44] E. Boaknin, M.A. Tanatar, J. Paglione, D. Hawthorn, F. Ronning, R.W. Hill, M. Sutherland, L. Taillefer, J. Sonier, S.M. Hayden, et al., Heat conduction in the vortex state of $NbSe_2$: Evidence for multiband superconductivity, Phys. Rev. Lett. 90 (11) (2003) 117003, http://dx.doi.org/10.1103/PhysRevLett.90.117003.

[45] I. Guillamon, H. Suderow, F. Guinea, S. Vieira, Intrinsic atomic-scale modulations of the superconducting gap of 2H-$NbSe_2$, Phys. Rev. B 77 (13) (2008) 134505, http://dx.doi.org/10.1103/PhysRevB.77.134505.

[46] D.J. Rahn, S. Hellmann, M. Kalläne, C. Sohrt, T.K. Kim, L. Kipp, K. Rossnagel, Gaps and kinks in the electronic structure of the superconductor 2H-$NbSe_2$ from angle-resolved photoemission at 1K, Phys. Rev. B 85 (22) (2012) 224532, http://dx.doi.org/10.1103/PhysRevB.85.224532.

[47] Y. Noat, J.A. Silva-Guillén, T. Cren, V. Cherkez, C. Brun, S. Pons, F. Debontridder, D. Roditchev, W. Sacks, L. Cario, et al., Quasiparticle spectra of 2H-$NbSe_2$: Two-band superconductivity and the role of tunneling selectivity, Phys. Rev. B 92 (13) (2015) 134510, http://dx.doi.org/10.1103/PhysRevB.92.134510.

[48] E. Piatti, J. Montagna Bozzone, D. Daghero, Anomalous metallic phase in molybdenum disulphide induced via gate-driven organic ion intercalation, Nanomaterials 12 (2022) 1842, http://dx.doi.org/10.3390/nano12111842.

[49] S.H.N. Lim, D.R. McKenzie, M.M.M. Bilek, Van der Pauw method for measuring resistivity of a plane sample with distant boundaries, Rev. Sci. Instrum. 80 (7) (2009) http://dx.doi.org/10.1063/1.3183503.

[50] D. Daghero, R.S. Gonnelli, Probing multiband superconductivity by point-contact spectroscopy, Supercond. Sci. Technol. 23 (4) (2010) 043001, http://dx.doi.org/10.1088/0953-2048/23/4/043001.

[51] D. Daghero, E. Piatti, N.D. Zhigadlo, G.A. Ummarino, N. Barbero, T. Shiroka, Superconductivity of underdoped PrFeAs(O, F) investigated via point-contact spectroscopy and nuclear magnetic resonance, Phys. Rev. B 102 (10) (2020) 104513, http://dx.doi.org/10.1103/PhysRevB.102.104513.

[52] D. Torsello, E. Piatti, G.A. Ummarino, X. Yi, X. Xing, Z. Shi, G. Ghigo, D. Daghero, Nodal multigap superconductivity in the anisotropic iron-based compound $RbCa_2Fe_4As_4F_2$, Npj Quantum Mater. 7 (1) (2022) 1–7, http://dx.doi.org/10.1038/s41535-021-00419-1.

[53] L. Boeri, R.G. Hennig, P.J. Hirschfeld, G. Profeta, A. Sanna, E. Zurek, W.E. Pickett, M. Amsler, R. Dias, M. Eremets, et al., The 2021 room-temperature superconductivity roadmap, J. Phys.: Condens. Matter. 34 (2022) 183002, http://dx.doi.org/10.1088/1361-648X/ac2864.

[54] N. Lu, P. Zhang, Q. Zhang, R. Qiao, Q. He, H.-B. Li, Y. Wang, J. Guo, D. Zhang, Z. Duan, et al., Electric-field control of tri-state phase transformation with a selective dual-ion switch, Nature 546 (7656) (2017) 124–128, http://dx.doi.org/10.1038/nature22389.

[55] Y. Meng, X. Xing, X. Yi, B. Li, N. Zhou, M. Li, Y. Zhang, W. Wei, J. Feng, K. Terashima, et al., Protonation-induced discrete superconducting phases in bulk FeSe single crystals, Phys. Rev. B 105 (2022) 134506, http://dx.doi.org/10.1103/PhysRevB.105.134506.

[56] Y. Saito, T. Nojima, Y. Iwasa, Quantum phase transitions in highly crystalline two-dimensional superconductors, Nat. Commun. 9 (1) (2018) 778, http://dx.doi.org/10.1038/s41467-018-03275-z.

[57] L. Li, C. Chen, K. Watanabe, T. Taniguchi, Y. Zheng, Z. Xu, V.M. Pereira, K.P. Loh, A.H. Castro Neto, Anomalous quantum metal in a 2D crystalline superconductor with electronic phase nonuniformity, Nano Lett. 19 (6) (2019) 4126–4133, http://dx.doi.org/10.1021/acs.nanolett.9b01574.

[58] G. Bergmann, Physical interpretation of weak localization: A time-of-flight experiment with conduction electrons, Phys. Rev. B 28 (6) (1983) 2914, http://dx.doi.org/10.1103/PhysRevB.28.2914.

[59] S. Barua, M.C. Hatnean, M.R. Lees, G. Balakrishnan, Signatures of the Kondo effect in VSe_2, Sci. Rep. 7 (1) (2017) 10964, http://dx.doi.org/10.1038/s41598-017-11247-4.

[60] B.L. Altshuler, A.G. Aronov, P.A. Lee, Interaction effects in disordered Fermi systems in two dimensions, Phys. Rev. Lett. 44 (19) (1980) 1288, http://dx.doi.org/10.1103/PhysRevLett.44.1288.

[61] H. Fukuyama, Electron–Electron Interactions in Disordered Systems, North Holland, Amsterdam, 1985.

[62] R. Bianco, M. Calandra, F. Mauri, Electronic and vibrational properties of $TiSe_2$ in the charge-density-wave phase from first principles, Phys. Rev. B 92 (9) (2015) 094107, http://dx.doi.org/10.1103/PhysRevB.92.094107.

[63] T. Rohwer, S. Hellmann, M. Wiesenmayer, C. Sohrt, A. Stange, B. Slomski, A. Carr, Y. Liu, L.M. Avila, M. Kalläne, et al., Collapse of long-range charge order tracked by time-resolved photoemission at high momenta, Nature 471 (7339) (2011) 490–493, http://dx.doi.org/10.1038/nature09829.

[64] G. Blatter, M.V. Feigel'man, V.B. Geshkenbein, A.I. Larkin, V.M. Vinokur, Vortices in high-temperature superconductors, Rev. Modern Phys. 66 (4) (1994) 1125, http://dx.doi.org/10.1103/RevModPhys.66.1125.

[65] P. Berghuis, P.H. Kes, Two-dimensional collective pinning and vortex-lattice melting in a-$Nb_{1-x}Ge_x$ films, Phys. Rev. B 47 (1) (1993) 262, http://dx.doi.org/10.1103/PhysRevB.47.262.

[66] M. Tinkham, Effect of fluxoid quantization on transitions of superconducting films, Phys. Rev. 129 (6) (1963) 2413, http://dx.doi.org/10.1103/PhysRev.129.2413.

[67] N.A. Lewellyn, I.M. Percher, J. Nelson, J. Garcia-Barriocanal, I. Volotsenko, A. Frydman, T. Vojta, A.M. Goldman, Infinite-randomness fixed point of the quantum superconductor-metal transitions in amorphous thin films, Phys. Rev. B 99 (5) (2019) 054515, http://dx.doi.org/10.1103/PhysRevB.99.054515.

[68] X. Wang, L. Wang, Y. Liu, F. Chen, W. Gao, Y. Wu, Z. Xu, W. Peng, Z. Wang, Z. Di, et al., Robust quantum griffiths singularity above 1.5 K in nitride thin films, Phys. Rev. B 107 (2023) 094509, http://dx.doi.org/10.1103/PhysRevB.107.094509.

[69] M.H. Theunissen, P.H. Kes, Resistive transitions of thin film superconductors in a magnetic field, Phys. Rev. B 55 (22) (1997) 15183, http://dx.doi.org/10.1103/PhysRevB.55.15183.

[70] S. Ullah, A.T. Dorsey, Critical fluctuations in high-temperature superconductors and the Ettingshausen effect, Phys. Rev. Lett. 65 (16) (1990) 2066, http://dx.doi.org/10.1103/PhysRevLett.65.2066.

[71] G. Dezi, N. Scopigno, S. Caprara, M. Grilli, Negative electronic compressibility and nanoscale inhomogeneity in ionic-liquid gated two-dimensional superconductors, Phys. Rev. B 98 (21) (2018) 214507, http://dx.doi.org/10.1103/PhysRevB.98.214507.

[72] G. Venditti, J. Biscaras, S. Hurand, N. Bergeal, J. Lesueur, A. Dogra, R.C. Budhani, M. Mondal, J. Jesudasan, P. Raychaudhuri, et al., Nonlinear I-V characteristics of two-dimensional superconductors: Berezinskii-Kosterlitz–Thouless physics versus inhomogeneity, Phys. Rev. B 100 (6) (2019) 064506, http://dx.doi.org/10.1103/PhysRevB.100.064506.

[73] Y. Xing, P. Yang, J. Ge, J. Yan, J. Luo, H. Ji, Z. Yang, Y. Li, Z. Wang, Y. Liu, et al., Extrinsic and intrinsic anomalous metallic states in transition metal dichalcogenide Ising superconductors, Nano Lett. 21 (18) (2021) 7486–7494, http://dx.doi.org/10.1021/acs.nanolett.1c01426.

[74] A. Gurevich, Enhancement of the upper critical field by nonmagnetic impurities in dirty two-gap superconductors, Phys. Rev. B 67 (18) (2003) 184515, http://dx.doi.org/10.1103/PhysRevB.67.184515.

[75] X. Xing, W. Zhou, J. Wang, Z. Zhu, Y. Zhang, N. Zhou, B. Qian, X. Xu, Z. Shi, Two-band and Pauli-limiting effects on the upper critical field of 112-type iron pnictide superconductors, Sci. Rep. 7 (1) (2017) 45943, http://dx.doi.org/10.1038/srep45943.

[76] D. Ding, Z. Qu, X. Han, C. Han, Q. Zhuang, X.-L. Yu, R. Niu, Z. Wang, Z. Li, Z. Gan, et al., Multivalley superconductivity in monolayer transition metal dichalcogenides, Nano Lett. 22 (2022) 7919–7926, http://dx.doi.org/10.1021/acs.nanolett.2c02947.

[77] Y.G. Naidyuk, I.K. Yanson, Point-Contact Spectroscopy, Springer New York, NY, 2005, http://dx.doi.org/10.1007/978-1-4757-6205-1.

[78] R.S. Gonnelli, D. Daghero, G.A. Ummarino, V.A. Stepanov, J. Jun, S.M. Kazakov, J. Karpinski, Direct evidence for two-band superconductivity in MgB_2 single crystals from directional point-contact spectroscopy in magnetic fields, Phys. Rev. Lett. 89 (24) (2002) 247004, http://dx.doi.org/10.1103/PhysRevLett.89.247004.

[79] R.S. Gonnelli, D. Daghero, A. Calzolari, G.A. Ummarino, V. Dellarocca, V.A. Stepanov, J. Jun, S.M. Kazakov, J. Karpinski, Magnetic-field dependence of the gaps in a two-band superconductor: A point-contact study of MgB_2 single crystals, Phys. Rev. B 69 (10) (2004) 100504, http://dx.doi.org/10.1103/PhysRevB.69.100504(R).

[80] D. Daghero, M. Tortello, G.A. Ummarino, R.S. Gonnelli, Directional point-contact Andreev-reflection spectroscopy of Fe-based superconductors: Fermi surface topology, Gap Symmetry, Electron–Boson Interact. Rep. Prog. Phys. 74 (12) (2011) 124509, http://dx.doi.org/10.1088/0034-4885/74/12/124509.

[81] D. Daghero, E. Piatti, N.D. Zhigadlo, R.S. Gonnelli, A model for critical current effects in point-contact Andreev-reflection spectroscopy, Low Temp. Phys. 49 (2023) 886–892, http://dx.doi.org/10.1063/10.0019702.

[82] G. Sheet, S. Mukhopadhyay, P. Raychaudhuri, Role of critical current on the point-contact Andreev reflection spectra between a normal metal and a superconductor, Phys. Rev. B 69 (2004) 134507, http://dx.doi.org/10.1103/PhysRevB.69.134507.

[83] T.Y. Chen, S.X. Huang, C.L. Chien, Pronounced effects of additional resistance in Andreev reflection spectroscopy, Phys. Rev. B 81 (2010) 214444, http://dx.doi.org/10.1103/PhysRevB.81.214444.

[84] S. Döring, S. Schmidt, S. Gottwals, F. Schmidl, V. Tympel, I. Mönch, F. Kurth, K. Iida, B. Holzapfel, P. Seidel, Influence of the spreading resistance on the conductance spectrum of planar hybrid thin film SNS' junctions based on iron pnictides, J. Phys. Conf. Ser. 507 (1) (2014) 012008, http://dx.doi.org/10.1088/1742-6596/507/1/012008.

[85] E. Piatti, D. Torsello, F. Breccia, T. Tamegai, G. Ghigo, D. Daghero, Superconductivity of Co-Doped $CaKFe_4As_4$ Investigated via Point-Contact Spectroscopy and London Penetration Depth Measurements, Nanomaterials 14 (15) (2024) 1319.

[86] S. Kashiwaya, Y. Tanaka, Tunnelling effects on surface bound states in unconventional superconductors, Rep. Progr. Phys. 63 (10) (2000) 1641, http://dx.doi.org/10.1088/0034-4885/63/10/202.

[87] S. Kashiwaya, Y. Tanaka, M. Koyanagi, K. Kajimura, Theory for tunneling spectroscopy of anisotropic superconductors, Phys. Rev. B 53 (1996) 2667–2676, http://dx.doi.org/10.1103/PhysRevB.53.2667.

[88] G.E. Blonder, M. Tinkham, T.M. Klapwijk, Transition from metallic to tunneling regimes in superconducting microconstrictions: Excess current, charge imbalance, and supercurrent conversion, Phys. Rev. B 25 (1982) 4515–4532, http://dx.doi.org/10.1103/PhysRevB.25.4515.

[89] K. Zhao, H. Lin, X. Xiao, W. Huang, W. Yao, M. Yan, Y. Xing, Q. Zhang, Z.-X. Li, S. Hoshino, et al., Disorder-induced multifractal superconductivity in monolayer niobium dichalcogenides, Nat. Phys. 15 (9) (2019) 904–910, http://dx.doi.org/10.1038/s41567-019-0570-0.

[90] H. Suhl, B. Matthias, L.R. Walker, Bardeen-Cooper-Schrieffer theory of superconductivity in the case of overlapping bands, Phys. Rev. Lett. 3 (12) (1959) 552, http://dx.doi.org/10.1103/PhysRevLett.3.552.

[91] G.A. Ummarino, M. Tortello, D. Daghero, R.S. Gonnelli, Three-band s±Eliashberg theory and the superconducting gaps of iron pnictides, Phys. Rev. B 80 (17) (2009) 172503, http://dx.doi.org/10.1103/PhysRevB.80.172503.

[92] G.A. Ummarino, R.S. Gonnelli, S. Massidda, A. Bianconi, Two-band Eliashberg equations and the experimental T_c of the diboride $Mg_{1-x}Al_xB_2$, Phys. C: Supercond. Appl. 407 (2004) 121–127, http://dx.doi.org/10.1016/j.physc.2004.05.009.

[93] D. Torsello, K. Cho, K.R. Joshi, S. Ghimire, G.A. Ummarino, N.M. Nusran, M.A. Tanatar, W.R. Meier, M. Xu, S.L. Bud'Ko, et al., Analysis of the London penetration depth in Ni-doped $CaKFe_4As_4$, Phys. Rev. B 100 (9) (2019) 094513, http://dx.doi.org/10.1103/PhysRevB.100.094513.

[94] M. Mansor, J.P. Carbotte, Upper critical field in two-band superconductivity, Phys. Rev. B 72 (2) (2005) 024538, http://dx.doi.org/10.1103/PhysRevB.72.024538.

[95] G.A. Ummarino, D. Daghero, M. Tortello, R.S. Gonnelli, Predictions of multiband s±strong-coupling Eliashberg theory compared to experimental data in iron pnictides, J. Supecond. Nov. Magn. 24 (2011) 247–253, http://dx.doi.org/10.1007/s10948-010-1006-3.

[96] M.D. Watson, O.J. Clark, F. Mazzola, I. Marković, V. Sunko, T.K. Kim, K. Rossnagel, P.D.C. King, Orbital-and k_z-selective hybridization of Se 4p and Ti 3d states in the charge density wave phase of $TiSe_2$, Phys. Rev. Lett. 122 (7) (2019) 076404, http://dx.doi.org/10.1103/PhysRevLett.122.076404.

[97] J. Jeong, J. Jeong, H.-J. Noh, S.B. Kim, H.-D. Kim, Electronic structure study of Cu-doped 1T-$TiSe_2$ by angle-resolved photoemission spectroscopy, Phys. C: Supercond. Appl. 470 (2010) S648–S650, http://dx.doi.org/10.1016/j.physc.2009.11.123.

[98] E. Piatti, D. De Fazio, D. Daghero, S.R. Tamalampudi, D. Yoon, A.C. Ferrari, R.S. Gonnelli, Multi-valley superconductivity in ion-gated MoS_2 layers, Nano Lett. 18 (8) (2018) 4821–4830, http://dx.doi.org/10.1021/acs.nanolett.8b01390.

[99] H. Zhang, C. Berthod, H. Berger, T. Giamarchi, A.F. Morpurgo, Band filling and cross quantum capacitance in ion-gated semiconducting transition metal dichalcogenide monolayers, Nano Lett. 19 (12) (2019) 8836–8845, http://dx.doi.org/10.1021/acs.nanolett.9b03667.

[100] E. Piatti, D. Romanin, R.S. Gonnelli, Mapping multi-valley Lifshitz transitions induced by field-effect doping in strained MoS_2 nanolayers, J. Phys.: Condens. Matter. 31 (11) (2019) 114002, http://dx.doi.org/10.1088/1361-648X/aaf981.